Geophysical Prospecting

EAGE EUROPEAN ASSOCIATION OF GEOSCIENTISTS & ENGINEERS

Geophysical Prospecting, 2018 doi: 10.1111/1365-2478.12700

Acoustic directional snapshot wavefield decomposition

Max Holicki*, Guy Drijkoningen and Kees Wapenaar

Department of Geoscience & Engineering, Delft University of Technology, Stevinweg 1, 2628 CN, Delft, the Netherlands

Received June 2018, revision accepted September 2018

ABSTRACT

Up–down wavefield decomposition is effectuated by a scaled addition or subtraction of the pressure and vertical particle velocity, generally on horizontal or vertical surfaces, and works well for data given on such surfaces. The method, however, is not applicable to decomposing a wavefield when it is given at one instance in time, i.e. on snapshots. Such situations occur when a wavefield is modelled with methods like finite-difference techniques, for the purpose of, for example, reverse time migration, where the entire wavefield is determined per time instance. We present an alternative decomposition method that is exact when working on snapshots of an acoustic wavefield in a homogeneous medium, but can easily be approximated to heterogeneous media, and allows the wavefield to be decomposed in arbitrary directions. Such a directional snapshot wavefield decomposition is achieved by recasting the acoustic system in terms of the time derivative of the pressure and the vertical particle velocity, as opposed to the vertical derivative in up–down decomposition for data given on a horizontal surface. As in up–down decomposition of data given at a horizontal surface, the system can be eigenvalue decomposed and the inverse of the eigenvector matrix decomposes the wavefield snapshot into fields of opposite directions, including up–down decomposition. As the vertical particle velocity can be rotated at will, this allows for decomposition of the wavefield into any spatial direction; even spatially varying directions are possible. We show the power and effectiveness of the method by synthetic examples and models of increasing complexity.

Key words: Acoustics, Multicomponent, Modelling, Seismics.

1 INTRODUCTION

Multicomponent acoustic directional wavefield decomposition separates acoustic wavefields according to their direction of propagation. This is useful when distinguishing between waves entering a medium from above, like surface-related multiples from above the acquisition surface, and waves leaving the medium from below, like the reflection data geophysicists are often interested in. In marine seismology, acoustic wavefield decomposition using arrays of receivers below the water surface allows for the removal of the receiver ghost, an event caused by the reflection of a recorded up-going wavefield at the sea-surface that is then recorded as a time-delayed down-going wavefield. This process is known as receiver deghosting (Barr and Sanders 1989). The removed receiver ghost can then be used as an additional source wavefield in processing, see Lu *et al.* (2015). Wavefield decomposition is also an important tool in acoustic imaging, where it is either a pre-requisite step before being able to image the subsurface (Wapenaar *et al.* 1990) or directly part of the imaging condition (Díaz and Sava 2015).

Historically, multicomponent wavefield decomposition is as old as the Poynting vector (Poynting 1884), introduced to exploration geophysics for the acoustic case by Yoon and

*E-mail: m.e.holicki@tudelft.nl

Marfurt (2006). Acoustic decomposition began in the 1960s when White (1965) developed the data-driven particle velocity to pressure filter matching in P-Z summation. This, however, was inexact and was followed by the development up–down decomposition for acoustic and elastic waves along horizontal recording surfaces by the likes of Frasier (1970), Aki and Richards (1980), Ursin (1983), Kennett (1984), Dankbaar (1985), Wapenaar *et al.* (1990). At the same time plane-wave up–down decomposition along a vertical array of receivers was developed by Suprajitno and Greenhalgh (1985) for homogeneous vertical seismic profiles in wells, shortly followed by parametric decomposition by Leaney and Schlumberger (1990). More recent work has focused on the use of analytic wavefields in the directional decomposition of wavefields, which only requires spatial Hilbert transforms in the direction of decomposition but comes at the cost of having to model an additional wavefield, see Shen and Albertin (2015).

Although most of the above techniques operate in the horizontal wavenumber–frequency domain for a constant depth, we propose to decompose acoustic wavefields in the full-wavenumber domain for a constant time, i.e. on snapshots of the wavefield. Since the decomposition is in the full-wavenumber domain, we call it a directional decomposition. So we directionally decompose snapshots of an acoustic wavefield as opposed to decomposing a wavefield recorded on a horizontal interface into up- and down-going fields. To achieve this we assume the components of the wavefield are known everywhere, like in modelling. As in Ursin (1983), our alternative method works by scaling a component of the particle-velocity vector to the scalar pressure, and subsequently adding or subtracting the two to effectuate the directional decomposition.

We will begin this work by discussing the scalar acoustic system for homogeneous time-invariant media in the wavenumber domain. To derive purely spatial acoustic decomposition operators we will reformulate the acoustic system in terms of two independent linear equations. The eigenvalue decomposition of this system will then yield eigenvectors that allow us to directionally decompose the system.

Next we will demonstrate that decomposition is not limited to one global decomposition direction and that the wavefield can be decomposed at arbitrary points in arbitrary directions by rotating the decomposition operator. We will finish by illustrating these operations on models with increasing complexity. Let us begin by reviewing the fundamentals of acoustic wavefield decomposition for homogeneous time-invariant media.

2 ACOUSTIC WAVEFIELD DECOMPOSITION

The three-dimensional (3D) source-free acoustic system, for time-invariant homogeneous media, is governed by the linearized equations of continuity and motion respectively (Aki and Richards 1980):

$$\partial_t p = -\rho c^2 \nabla \cdot \mathbf{v}, \tag{1}$$

$$\partial_t \mathbf{v} = -\frac{1}{\rho} \nabla p, \tag{2}$$

where ∂_t is the temporal derivative along time t, $p(\mathbf{x}, t)$ is the acoustic pressure difference to the time- and space-independent background pressure, c is the time-independent acoustic velocity, ρ is the time-independent bulk density, ∇ is the del, or nabla, operator differentiating along all spatial dimensions with spatial coordinates $\mathbf{x}$, $\cdot$ denotes the vector dot product and $\mathbf{v}(\mathbf{x}, t)$ is the particle-velocity vector. Note that vectors are denoted using bold lower-case symbols, while matrices are upper-case and bold.

Equations (1) and (2) are written in Cartesian coordinates, with no preferential direction prescribed. For the following directional decomposition of acoustic waves, a preferential direction must be chosen; in geophysics this is often the vertical. We will denote this preferential direction with a subscript z, denoting an arbitrary direction.

We will now transform equations (1) and (2) to the 3D wavenumber-time domain. To this end we define the 3D wavenumber Fourier transform as the Fourier transform over all spatial dimensions of a function $f(\mathbf{x}, t)$ as:

$$\tilde{f}(\mathbf{k}, t) = \int_{\mathbb{R}^3} f(\mathbf{x}, t) \mathrm{e}^{i\mathbf{x}\cdot\mathbf{k}} \mathrm{d}\mathbf{x} = \mathcal{F}_{\mathbf{x}} f(\mathbf{x}, t), \tag{3}$$

where $\mathbf{k}$ is the vector of wavenumbers, or Fourier parameters, corresponding to the spatial coordinates $\mathbf{x}$, $\mathbb{R}^3$ is the set of real 3D coordinates and $i = \sqrt{-1}$ is the imaginary unit. $\mathcal{F}_{\mathbf{x}}$ denotes the forward Fourier transform operator. Note that tildes are used to denote quantities in the 3D wavenumber-time domain.

With these assumptions we transform the source-free acoustic system, equations (1) and (2), to the wavenumber-time domain, in which the system is decomposed into spatial plane waves:

$$\partial_t \tilde{p} = \rho c^2 i \mathbf{k} \cdot \tilde{\mathbf{v}}, \tag{4}$$

$$\partial_t \tilde{\mathbf{v}} = \frac{i\mathbf{k}}{\rho} \tilde{p}. \tag{5}$$

The corresponding acoustic pressure wave equation, found by inserting equation (5) into (4), is

$$\partial_t^2 \tilde{p} = -c^2 \mathbf{k} \cdot \mathbf{k} \tilde{p}. \tag{6}$$

We now wish to decompose the wavefield into a specific direction and its opposite direction. Usually this is accomplished by writing the acoustic system in terms of the pressure and the particle velocity in the direction of decomposition, the z direction. To express equation (4) in terms of $\tilde{v}_z$ we back substitute $\tilde{v}_z$ from equation (5) into equation (6) and integrate over time for a zero constant of integration:

$$\partial_t \tilde{p} = \rho c^2 \frac{\mathbf{k} \cdot \mathbf{k}}{-ik_z} \tilde{v}_z \quad \text{for } k_z \neq 0. \tag{7}$$

Note that in this paper we do not use Einstein's summation convention for repeated subscripts.

Equation (7) only holds for $k_z \neq 0$; for $k_z = 0$, waves are travelling orthogonally to the z direction and are not accounted for in $\tilde{v}_z$. To resolve this undefined behaviour for $k_z = 0$ we have two options. We can zero the fraction for $k_z = 0$, which implicitly assumes the absence of waves travelling orthogonally to the z direction as all $\mathbf{k}$ are assumed to be zero for all $k_z = 0$, which is generally not the case. Alternatively, we can express the fraction for $k_z = 0$ in terms of orthogonal wavenumber components. For the moment we assume the former, however, in Subsection 2.3 we will discuss how to include orthogonal wavenumber components.

We can now combine equation (7) with equation (5) to find the following system in terms of $\tilde{p}$ and $\tilde{v}_z$:

$$\partial_t \begin{pmatrix} \tilde{p} \\ \tilde{v}_z \end{pmatrix} = \begin{pmatrix} 0 & \rho c^2 \frac{\mathbf{k} \cdot \mathbf{k}}{-ik_z} \\ \frac{ik_z}{\rho} & 0 \end{pmatrix} \begin{pmatrix} \tilde{p} \\ \tilde{v}_z \end{pmatrix}. \tag{8}$$

In matrix–vector notation we can write this as:

$$\partial_t \tilde{\mathbf{q}}_z = \tilde{\mathbf{A}}_z \tilde{\mathbf{q}}_z, \tag{9}$$

where

$$\tilde{\mathbf{q}}_z = \begin{pmatrix} \tilde{p} \\ \tilde{v}_z \end{pmatrix}, \tag{10}$$

$$\tilde{\mathbf{A}}_z = \begin{pmatrix} 0 & \rho c^2 \frac{\mathbf{k} \cdot \mathbf{k}}{-ik_z} \\ \frac{ik_z}{\rho} & 0 \end{pmatrix}, \tag{11}$$

where the subscripts indicate to which particle-velocity component $\tilde{\mathbf{q}}$ and $\tilde{\mathbf{A}}$ are related to.

Equation (9) represents a different starting point for directional decomposition than conventional up–down decomposition, see Ursin (1983) for example. In conventional decomposition the system is written with $\partial_z \mathbf{q}_z$ on the left-hand side, whereas here we have $\partial_t \mathbf{q}_z$.

2.1 Eigenvalue decomposition

Decomposing $\tilde{\mathbf{A}}$ into an eigenvalue matrix $\tilde{\mathbf{\Lambda}}$ and eigenvector matrix $\tilde{\mathbf{L}}$ we have:

$$\partial_t \tilde{\mathbf{q}}_z = \tilde{\mathbf{L}} \tilde{\mathbf{\Lambda}} \tilde{\mathbf{L}}^{-1} \tilde{\mathbf{q}}_z, \tag{12}$$

where we have for a judicial choice of the z direction as the principal direction and pressure normalization of the eigenvectors:

$$\tilde{\mathbf{\Lambda}}_z = ci \, \mathrm{sgn}(k_z) ||\mathbf{k}|| \begin{pmatrix} 1 & 0 \\ 0 & -1 \end{pmatrix}, \tag{13}$$

$$\tilde{\mathbf{L}}_{p,z} = \begin{pmatrix} 1 & 1 \\ \frac{1}{\rho c} \frac{|k_z|}{||\mathbf{k}||} & -\frac{1}{\rho c} \frac{|k_z|}{||\mathbf{k}||} \end{pmatrix}, \tag{14}$$

where sgn() is the signum function corresponding to a quantity divided by its magnitude $||$. Note that the subscript z indicates that the signs of the eigenvalues were chosen according to the sign of k_z. The subscript p is used to denote pressure-normalized eigenvectors, as opposed to the particle-velocity-normalized eigenvectors that are shown later in Subsection 2.4.

We now define the decomposed fields $\tilde{\mathbf{d}}$ as the result of a general eigenvector matrix inverse $\tilde{\mathbf{L}}^{-1}$ acting on $\tilde{\mathbf{q}}$:

$$\tilde{\mathbf{d}} = \tilde{\mathbf{L}}^{-1} \tilde{\mathbf{q}}, \tag{15}$$

where for the pressure-normalized z-direction case:

$$\tilde{\mathbf{L}}_{p,z}^{-1} = \frac{1}{2} \begin{pmatrix} 1 & \rho c \frac{||\mathbf{k}||}{|k_z|} \\ 1 & -\rho c \frac{||\mathbf{k}||}{|k_z|} \end{pmatrix}. \tag{16}$$

Rearranging equation (12) with the help of equation (15) and the assumption that the medium parameters are time invariant we find:

$$\partial_t \tilde{\mathbf{d}} = \tilde{\mathbf{\Lambda}} \tilde{\mathbf{d}}. \tag{17}$$

We have now decomposed the acoustic wave equation into two first-order-in-time independent equations. Note that in equation (17) we have not specified a direction or normalization.

To better understand equation (17) let us look at its components in more detail for the case of choosing the signs according to the z direction. We can rewrite equation (13) as

the following by expressing $||\mathbf{k}||$ in terms of $|k_z|$ and the acute angle $\tilde{\theta}_z$ between them:

$$\tilde{\mathbf{\Lambda}}_z = ik_z \frac{c}{\cos(\tilde{\theta}_z)} \begin{pmatrix} 1 & 0 \\ 0 & -1 \end{pmatrix}, \tag{18}$$

where

$$i\,\mathrm{sgn}(k_z)||\mathbf{k}|| = \frac{ik_z}{\cos(\tilde{\theta}_z)}, \tag{19}$$

and

$$\tilde{\theta}_z = \mathrm{arctan3}(k_x, |k_z|), \tag{20}$$

$$\text{where } -\frac{\pi}{2} < \tilde{\theta}_z \leq \frac{\pi}{2},$$

where we define arctan3(), which is similar to the common arctan2() variant, to be the following variant of the arctangent:

$$\mathrm{arctan3}(x,z) = \begin{cases} \arctan(\frac{x}{z}) & \text{if } z > 0, \\ \arctan(\frac{x}{z}) + \pi & \text{if } z < 0 \quad \text{and} \quad x \geq 0, \\ \arctan(\frac{x}{z}) - \pi & \text{if } z < 0 \quad \text{and} \quad x < 0, \\ +\frac{\pi}{2} & \text{if } z = 0 \quad \text{and} \quad x \neq 0, \\ \text{undefined} & \text{if } z = 0 \quad \text{and} \quad x = 0. \end{cases} \tag{21}$$

Again care must be taken for waves travelling in the orthogonal directions, as for these $\cos(\tilde{\theta}_i) = 0$ or undefined at the origin in the wavenumber domain, where the pressure and particle velocity must be zero. The pressure p must be zero since we assumed that it is measured with respect to the homogeneous time-invariant background pressure and the particle velocity must be zero such that the system as a whole is at rest, as this was assumed when deriving the acoustic wave equation (Aki and Richards 1980). We again zero the operation, like for equation (7), for $k_z = 0$.

Based on equation (18), $\tilde{\mathbf{\Lambda}}$ corresponds to a modified derivative in the space domain in the z direction, due to the ik_z, however via equation (17) the action of $\tilde{\mathbf{\Lambda}}$ is also equivalent to the time derivative. $\tilde{\mathbf{\Lambda}}$ evidently expresses the time derivative in terms of spatial derivatives.

With the judicious choice of normalization for $\tilde{\mathbf{L}}_{p,z}$ in equation (16), the decomposed fields $\tilde{\mathbf{d}}_{p,z}$, equation (15), can be interpreted as pressure wavefields:

$$\tilde{\mathbf{d}}_{p,z} = \begin{pmatrix} \tilde{p}_z^+ \\ \tilde{p}_z^- \end{pmatrix} = \frac{1}{2} \begin{pmatrix} 1 & \rho c \frac{||\mathbf{k}||}{|k_z|} \\ 1 & -\rho c \frac{||\mathbf{k}||}{|k_z|} \end{pmatrix} \begin{pmatrix} \tilde{p} \\ \tilde{v}_z \end{pmatrix}. \tag{22}$$

Because the pressure-normalized form of the eigenvectors is used we denote the decomposed fields in terms of the pressure wavefields p_z^+ and p_z^-. We can further express equation (22) in terms of $\tilde{\theta}_i$ via equation (19) as:

$$\begin{pmatrix} \tilde{p}_z^+ \\ \tilde{p}_z^- \end{pmatrix} = \frac{1}{2} \begin{pmatrix} 1 & \frac{\rho c}{\cos(\tilde{\theta}_z)} \\ 1 & -\frac{\rho c}{\cos(\tilde{\theta}_z)} \end{pmatrix} \begin{pmatrix} \tilde{p} \\ \tilde{v}_z \end{pmatrix}. \tag{23}$$

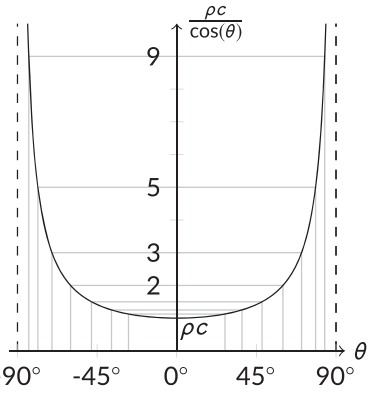

Figure 1 Acoustic wavefield decomposition scale factor for the z component of the particle velocity to the pressure with respect to the angle the corresponding plane wave makes with the z direction. To aid the reader the scale factors of 1.125, 1.25, 1.5, 2, 3, 5 and 9 times the specific acoustic impedance ρc are indicated in grey.

To better understand equation (23) consider Fig. 1, which shows how the scale factor of the decomposition depends on the angle $\tilde{\theta}$. For waves travelling at small angles to the z direction the scale factor is dominated by the local specific acoustic impedance, however as the wave begins to travel more and more obliquely to the z direction the scale factor grows asymptotically to infinity.

This asymptotic behaviour is due to the fact that we chose to approximate the acoustic system in terms of one component of the particle velocity. We can however recast the system in a more stable form that accounts for the asymptotic scaling by writing the system in terms of the magnitude of the full particle-velocity vector.

2.2 Formulation in terms of the full particle-velocity vector

The asymptotic behaviour and the associated singularities in Fig. 1 are due to the fraction in equation (22). We now wish to write the action of the wavenumber fraction on $\tilde{v}_z$ in terms of the magnitude of the particle-velocity vector. To do so we write the scaled z component of the particle velocity in in equation (22) in terms of its sign and absolute value:

$$\frac{||\mathbf{k}||}{|k_z|}\tilde{v}_z = \mathrm{sgn}(\tilde{v}_z) \left|\left| \frac{\mathbf{k}}{k_z}\tilde{v}_z \right|\right|. \tag{24}$$

Note that the signum of a complex quantity is that quantity divided by its magnitude. To interpret the magnitude term we return to the linearized equation of motion, equation (5), and solve for the pressure in terms of the jth and kth component of the particle velocity:

$$\tilde{p} = \frac{\rho}{ik_j}\partial_t \tilde{v}_j = \frac{\rho}{ik_k}\partial_t \tilde{v}_k \quad \text{for } k_j \neq 0 \quad \text{and} \quad k_k \neq 0. \tag{25}$$

Note that the second term in equation (25) is not valid for $k_j = 0$, while the last term is not valid for $k_k = 0$. Evidently different particle-velocity components, which are not necessarily orthogonal, can account for wavenumber components that another cannot account for and vice versa.

We can use equation (25) to write the particle-velocity vector in terms of the z component:

$$\tilde{\mathbf{v}} = \frac{\mathbf{k}}{k_z}\tilde{v}_z \quad \text{for } k_z \neq 0. \tag{26}$$

Based on the above it becomes evident that the magnitude term in equation (24) corresponds to the magnitude of the particle-velocity vector:

$$\frac{||\mathbf{k}||}{|k_z|}\tilde{v}_z = \text{sgn}(\tilde{v}_z)||\tilde{\mathbf{v}}||. \tag{27}$$

With this equation we can remove the asymptotic behaviour from equation (22) by writing it in terms of the magnitude of the particle velocity:

$$\begin{pmatrix} \tilde{p}_z^+ \\ \tilde{p}_z^- \end{pmatrix} = \frac{1}{2}\begin{pmatrix} 1 & \rho c \\ 1 & -\rho c \end{pmatrix}\begin{pmatrix} \tilde{p} \\ \text{sgn}(\tilde{v}_z)||\tilde{\mathbf{v}}|| \end{pmatrix}. \tag{28}$$

Equation (28) now does not show any singular behaviour and is unconditionally stable.

2.3 Accounting for $k_z = 0$

Recall that for equation (7) we chose to zero the operator for $k_z = 0$. This implicitly excludes the part of the wavefield where $k_z = 0$ but $\mathbf{k} \neq \mathbf{0}$, where $\mathbf{0}$ is the null vector. The consequence of this is that the eigenvalue decomposition does not hold for $k_z = 0$, because our sign choice for the eigenvalues is incomplete. Furthermore the elements in the second column of the matrix in equation (16) are zero, causing wavefields travelling orthogonally to the z direction to be equally split between the decomposed fields for $k_z = 0$. This remains a problem in equation (28) as $\tilde{v}_z = 0$ where $k_z = 0$. We will now correct for this by including the absent orthogonal information in equation (7).

To introduce the orthogonal wavefield information into equation (7), we recall from equation (25) that although no individual component of the particle velocity can properly account for the total pressure field, an orthogonal set of particle-velocity components can. Noting that the equation of motion, equation (5), dictates that any component of the particle velocity is zero where its corresponding wavenumber is zero, we now seek an equivalent to the z component of the particle velocity that where $k_z = 0$ is equal to the other components of the particle velocity.

To do so we must make a choice on how to order the dimensions. We introduce a generalized particle velocity $\tilde{v}_z$ that is equal to $\tilde{v}_z$ everywhere where $k_z \neq 0$. When $k_z = 0$, $\tilde{v}_z$ is equal to the first orthogonal component $\tilde{v}_x$ as long as $k_x \neq 0$, at which point $\tilde{v}_z$ is equal to $\tilde{v}_y$. At the origin in the wavenumber domain the generalized particle velocity is zero as each component of the particle velocity at the origin must be zero such that the acoustic system as a whole is at rest. The choice of how to order the particle velocity components where $k_z = 0$ is important because it defines how orthogonally travelling waves are mapped into the decomposed fields. Note that we should indicate either in the subscript or superscript of $\tilde{v}_z$ how the dimensions are ordered; we will assume that the ordering is always chosen using the same system and hence will not indicate the order of dimensions.

We now define the generalized particle velocity $\tilde{v}_z$ in three orthogonal dimensions (x, y, z) as:

$$\tilde{v}_z = \begin{cases} \tilde{v}_z & \text{if } k_z \neq 0, \\ \tilde{v}_x & \text{if } k_x \neq 0 \quad \text{and} \quad k_z = 0, \\ \tilde{v}_y & \text{if } k_y \neq 0 \quad \text{and} \quad k_z = k_x = 0, \\ 0 & \text{if } \mathbf{k} = \mathbf{0}. \end{cases} \tag{29}$$

The wavenumber κ_z associated with this generalized particle velocity that accounts for the orthogonal components we define as:

$$\kappa_z = \begin{cases} k_z & \text{if } k_z \neq 0 \\ k_x & \text{if } k_x \neq 0 \quad \text{and} \quad k_z = 0, \\ k_y & \text{if } k_y \neq 0 \quad \text{and} \quad k_z = k_x = 0, \\ 0 & \text{if } \mathbf{k} = \mathbf{0}. \end{cases} \tag{30}$$

Note that division by κ_z is still poorly defined at the origin in the wavenumber domain. When either the pressure or a particle-velocity component is divided by κ_z the result at the origin is assumed to be zero. This comes from our definition of the pressure being measured with respect to the time- and space-invariant background pressure. The particle velocity on the other hand must be zero at the origin in the wavenumber domain such that the acoustic system is globally at rest and not travelling as a whole in some direction, which would invalidate the original derivation of the acoustic system.

We can now, analogously to equation (26), fully express any particle-velocity component in terms of this generalized particle velocity $\tilde{v}_z$ and its associated wavenumber κ_z via:

$$\tilde{\mathbf{v}} = \frac{\mathbf{k}}{\kappa_z}\tilde{v}_z. \tag{31}$$

In order to find the acoustic system in terms of the generalized particle velocity $\tilde{v}_z$ we insert equation (31) into equations (4) and (5):

$$\partial_t \tilde{p} = \rho c^2 \frac{\mathbf{k}\cdot\mathbf{k}}{-i\kappa_z}\tilde{v}_z, \tag{32}$$

$$\partial_t \tilde{v}_z = \frac{i\kappa_z}{\rho}\tilde{p}. \tag{33}$$

Note that equation (32) is now well defined everywhere.

From here the derivation of wavefield decomposition is identical to the earlier derivation in terms of $\tilde{v}_z$ and will not be repeated here. The only difference is that we replace $\tilde{v}_z$ with $\tilde{v}_z$ and k_z with κ_z.

In terms of the generalized particle-velocity vector, the pressure-normalized decomposition, equation (22), reads:

$$\begin{pmatrix}\tilde{p}_z^+\\ \tilde{p}_z^-\end{pmatrix} = \frac{1}{2}\begin{pmatrix}1 & \rho c\dfrac{||\mathbf{k}||}{|\kappa_z|}\\ 1 & -\rho c\dfrac{||\mathbf{k}||}{|\kappa_z|}\end{pmatrix}\begin{pmatrix}\tilde{p}\\ \tilde{v}_z\end{pmatrix}. \tag{34}$$

The decomposition operator is now no longer undefined where $k_z = 0$.

We can remove the wavenumber scaling from equation (34) by writing it in terms of the magnitude of the particle-velocity vector:

$$\begin{pmatrix}\tilde{p}_z^+\\ \tilde{p}_z^-\end{pmatrix} = \frac{1}{2}\begin{pmatrix}1 & \rho c\\ 1 & -\rho c\end{pmatrix}\begin{pmatrix}\tilde{p}\\ \mathrm{sgn}(\tilde{v}_z)||\tilde{\mathbf{v}}||\end{pmatrix}. \tag{35}$$

This form of the decomposition is unconditionally stable and fully satisfies equation (17) with the eigenvalue matrix from equation (13), but now in terms of κ_z, where the eigenvalues additionally account for orthogonally travelling waves.

The only major difference between decomposition in terms of $\tilde{v}_z$ and $\tilde{v}_z$ is how orthogonally travelling waves are decomposed, which occur where $k_z = 0$. These are decomposed according to the orthogonal directions. This means that if z corresponds to the vertical direction, then the orthogonally travelling waves are for example left-right decomposed, instead of being neglected and equally split up between the decomposed fields, as occurs in the previous derivation, see Fig. 2.

This warrants a new nomenclature for the decomposition operators as the notion of up–down decomposition is inherently non-unique for $k_z = 0$. We choose to speak of (up-left)-(down-right) decomposition as opposed to simple up–down decomposition. In (up-left)-(down-right) decomposition we would map the purely left-going waves to the 'up-going' decomposed field, while purely right going waves get mapped to the 'down-going' field, or vice versa for (up-right)-(down-left) decomposition.

2.4 Particle-velocity-normalized decomposition

When we applied eigenvalue decomposition to equation (9) in Subsection 2.1 we chose to normalize the eigenvectors such that the inverse of the eigenvector matrix scaled the particle velocity to the pressure, hence the name pressure-normalized decomposition. It is also possible to choose the eigenvectors such that the pressure is scaled to the particle velocity. The resulting decomposition is known as the particle-velocity-normalized decomposition:

$$\tilde{\mathbf{d}}_{v,z} = \begin{pmatrix}\tilde{v}_z^+\\ \tilde{v}_z^-\end{pmatrix} = \frac{1}{2}\begin{pmatrix}\dfrac{1}{\rho c}\dfrac{|\kappa_z|}{||\mathbf{k}||} & 1\\ -\dfrac{1}{\rho c}\dfrac{|\kappa_z|}{||\mathbf{k}||} & 1\end{pmatrix}\begin{pmatrix}\tilde{p}\\ \tilde{v}_z\end{pmatrix}. \tag{36}$$

Note that equation (36) in conjunction with equation (22) implicitly means that we can change between pressure- and particle-velocity-normalized decomposed wavefields:

$$\begin{pmatrix}\tilde{v}_z^+\\ \tilde{v}_z^-\end{pmatrix} = \frac{|\kappa_z|}{\rho c||\mathbf{k}||}\begin{pmatrix}1 & 0\\ 0 & -1\end{pmatrix}\begin{pmatrix}\tilde{p}_z^+\\ \tilde{p}_z^-\end{pmatrix}. \tag{37}$$

These normalizations play an important role later in Fig. 7, where they are indirectly used to decompose already decomposed fields along another direction.

2.5 Rotating the decomposition direction

So far decomposition only occurred along the arbitrary z direction, along which the particle velocity was also recorded. We now wish to decompose the wavefield in some other direction defined by the angle vector $\boldsymbol{\phi}'$ with respect to the z direction. We have two options to achieve this: (1) We rotate the coordinate system such that the z direction points in the desired direction, which means that we also rotate the particle-velocity vector, and apply the same decomposition operator again, but in the new coordinate system. Or, (2) we can rotate the decomposition operator to decompose in the desired direction.

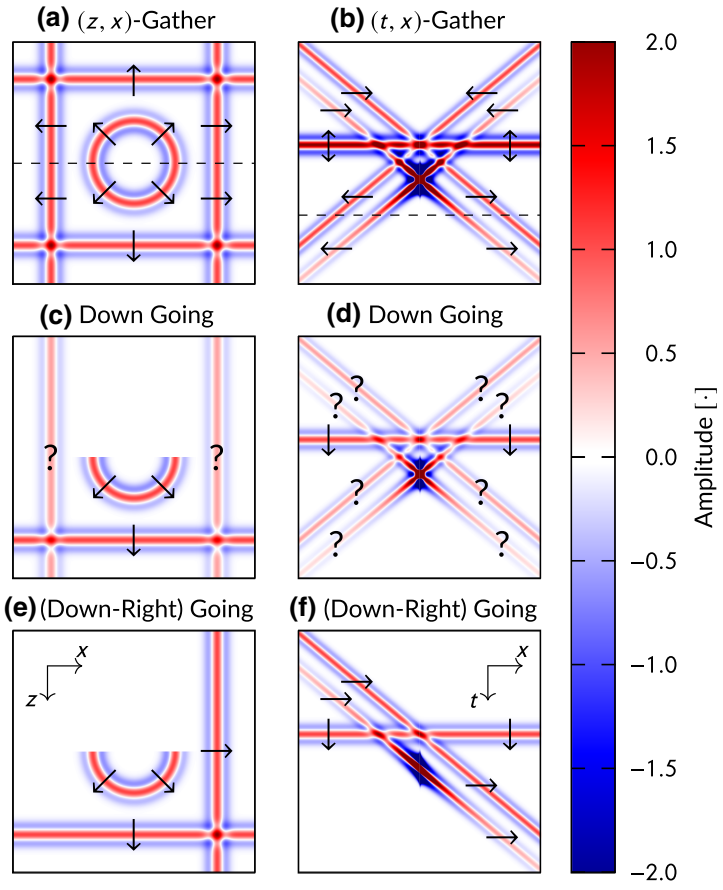

Figure 2 (a) (z, x) and (b) (t, x) gathers of a three-dimensional wavefield, for $t = 0$ and $z = 0$ respectively. Arrows indicate local propagation direction, and the dashed lines indicate their intersection. (c) and (d) show the down-going wavefields in (a) and (b) respectively, after decomposing without properly taking into account horizontally travelling waves. (e) and (f) are properly (up-left)-(down-right) decomposed versions of (a) and (b). Note how the horizontally travelling plane waves are both included with half amplitude in (c) and (d) and have unknown propagation directions, indicated by ?s. In (e) and (f), however, only the right-going plane wave is included and has a known propagation direction. Note that data at the spatial origin have been muted and that the coordinate system displayed in (e) applies to (a, c and e) and the coordinate system in (f) applies to (b, d and f).

For the first option we need to rotate the wavefield vector $\tilde{\mathbf{q}}_z$, with generalized particle-velocity component v_z, to point in the rotated z' direction. We recall that equation (25) allowed us to express not necessarily orthogonal components of the particle velocity in terms of each other. We can also use it to rotate the generalized particle velocity as follows:

$$\tilde{v}_{z'} = \frac{\kappa_{z'}}{\kappa_z}\tilde{v}_z, \tag{38}$$

where we chose to rotate $\mathbf{k}$ by ϕ' to find $k_{z'}$ and the associated $\kappa_{z'}$. Rotating $\tilde{\mathbf{q}}_z$ to $\tilde{\mathbf{q}}_{z'}$ then is

$$\tilde{\mathbf{q}}_{z'} = \begin{pmatrix} \tilde{p} \\ \tilde{v}_{z'} \end{pmatrix} = \begin{pmatrix} 1 & 0 \\ 0 & \frac{\kappa_{z'}}{\kappa_z} \end{pmatrix} \begin{pmatrix} \tilde{p} \\ \tilde{v}_{z'} \end{pmatrix} = \tilde{\mathbf{R}}\tilde{\mathbf{q}}_z. \tag{39}$$

Note that if equation (39) is transformed back to the space domain it simply corresponds to only rotating the particle-velocity vector, leaving the pressure untouched as it is direction independent.

When we decompose the acoustic system again using the new coordinate system and signing the magnitude of the particle-velocity vector according to $\kappa_{z'}$ instead of κ_z then we decompose along the z' direction. Mathematically we write the decomposition, analogously to equation (15), in the rotated coordinate system as:

$$\tilde{\mathbf{d}}_{z'} = \tilde{\mathbf{L}}_{z'}^{-1}\tilde{\mathbf{q}}_{z'}. \tag{40}$$

To rotate the decomposition operator instead of the particle velocity we back substitute equation (39) into (40) to find:

$$\tilde{\mathbf{d}}_{z'} = \tilde{\mathbf{L}}_{z'}^{-1}\tilde{\mathbf{R}}\tilde{\mathbf{q}}_z. \tag{41}$$

We can now include the rotation operator into the decomposition operator to find the rotated decomposition operator, which is a function of the angle vector $\boldsymbol{\phi}$ as it works for any angle. For the pressure normalized case, equation (16), it would be:

$$\tilde{\mathbf{L}}_{p,z}^{-1}(\boldsymbol{\phi}) = \tilde{\mathbf{L}}_{p,z'}^{-1}\tilde{\mathbf{R}} = \frac{1}{2}\begin{pmatrix} 1 & \rho c\frac{\mathrm{sgn}(\kappa(\boldsymbol{\phi}))||\mathbf{k}||}{\mathrm{sgn}(\kappa_z)|\kappa_z|} \\ 1 & -\rho c\frac{\mathrm{sgn}(\kappa(\boldsymbol{\phi}))||\mathbf{k}||}{\mathrm{sgn}(\kappa_z)|\kappa_z|} \end{pmatrix}, \tag{42}$$

where $\kappa(\boldsymbol{\phi})$ is the rotated κ_z in the new coordinate system. We have now rotated the decomposition operator such that it uses a particle-velocity component pointing in one direction but directionally decomposes the wavefield along another.

Equation (42) also demonstrates that the decomposition direction is purely determined by the sign choice for $|\mathbf{k}|$, and not by the chosen particle-velocity component, which is accounted for in the denominators.

We can also use equation (42) to make the *a priori* choice of the decomposition direction *a posterior* choice by extending the dimensionality of the operator output to additionally depend on the decomposition direction:

$$\tilde{\mathbf{d}}(\mathbf{k}, \mathbf{t}, \phi) = \tilde{\mathbf{L}}_z^{-1}(\mathbf{k}, \boldsymbol{\phi})\tilde{\mathbf{q}}_z(\mathbf{k}, \mathbf{t}). \tag{43}$$

Now the decomposed wavefields $\tilde{\mathbf{d}}$ are decomposed along all possible directions. We effectively treat the inherent directional ambiguity of the decomposition in terms of additional dimensions and at the cost of associated work. Note that this does not fully treat the ambiguity in sign choice for $|\kappa_z|$ as we only deal with the subset of sign choices that leads to directionally decomposed wavefields. Furthermore for each $\boldsymbol{\phi}$ the decomposition is still a global operation in space. In the next section we discuss spatially varying decomposition directions.

2.6 Spatially varying decomposition directions

To have spatially varying decomposition directions we need to transform the decomposition back to the space domain and then choose a different decomposition direction at each point in the space domain. Note that this also means that the decomposition direction can change in time.

This is trivial with equation (43). One can transform the decomposed results back to the space domain and then choose a different decomposition direction for every point in space and time. Mathematically this corresponds to extracting a $\boldsymbol{\phi} = \boldsymbol{\phi}'(\mathbf{x}, t)$ surface from the decomposed result of equation (43) in the space domain.

Taking things step by step we first need to transform equation (43) back to the space domain:

$$\mathbf{d}(\mathbf{x}, t, \boldsymbol{\phi}) = \mathcal{F}_{\mathbf{x}}^{-1}\tilde{\mathbf{L}}_z^{-1}(\mathbf{k}, \boldsymbol{\phi})\mathcal{F}_{\mathbf{x}}\mathbf{q}_z(\mathbf{x}, t). \tag{44}$$

To be able to extract a $\boldsymbol{\phi}'$ surface from equation (44) we need to make the decomposition direction a function of space and time. A simple static-in-time two-dimensional directional surface could be the radial direction away from some point, the origin for simplicity:

$$\phi'(x, z) = \text{arctan2}(x, z), \tag{45}$$

where arctan2 is the following variant of the arctangent:

$$\text{arctan2}(x, z) = \begin{cases} \arctan(\frac{x}{z}) & \text{if } z > 0, \\ \arctan(\frac{x}{z}) + \pi & \text{if } z < 0 \quad \text{and} \quad x \geq 0, \\ \arctan(\frac{x}{z}) - \pi & \text{if } z < 0 \quad \text{and} \quad x < 0, \\ +\frac{\pi}{2} & \text{if } z = 0 \quad \text{and} \quad x > 0, \\ -\frac{\pi}{2} & \text{if } z = 0 \quad \text{and} \quad x < 0, \\ \text{undefined} & \text{if } z = 0 \quad \text{and} \quad x = 0. \end{cases} \tag{46}$$

Note that at the wavenumber-domain origin, where ϕ' is undefined, we are free to define ϕ' to point in any direction, for example the z direction.

Note that any other conceivable, not necessarily smooth, surface is also acceptable. This particular choice of directional surface is of interest, though, because it decomposes wavefields into a wavefield collapsing towards a point and a wavefield expanding away from said point. If we now extract this surface from equation (44) we find:

$$\mathbf{d}_{\phi'}(\mathbf{x}, t) = \mathbf{d}(\mathbf{x}, t, \phi'(x, t)). \tag{47}$$

Note that depending on how orthogonal directions are treated in the decomposition, waves travelling at a given point tangential to the clockwise direction around the centre belong to the outward-going wavefield, while waves travelling counter-clockwise belong to the inward-going wavefield. Notice that we no longer speak of down- and up-going waves; we now have to speak of waves going inwards and waves going outwards due to our choice of decomposition direction.

This example is demonstrated in Fig. 3, in which an expanding and a collapsing wavefield (Fig. 3a) are separated by decomposing the wavefield into a wavefield travelling towards the centre and one travelling away from it (Fig. 3c). To aid in the visual inspection of the decomposition, the impedance-scaled particle velocity $\rho c v_{\phi'}$ measured in the directions defined by ϕ' is also included in Fig. 3(b). The associated desired decomposition angles are shown in Fig. 3(d).

The workflow for decomposing snapshots of an acoustic wavefield using spatially and possibly temporally varying wavefields is illustrated in Fig 4. The basic idea is to decompose snapshots of a wavefield everywhere in space for all desired decomposition directions, and then from the result to extract the desired decomposed fields in space and time. Note that extraction in other domains, like the wavenumber and/or frequency domains, may be fruitful, although the results may no longer be perfectly directionally decomposed.

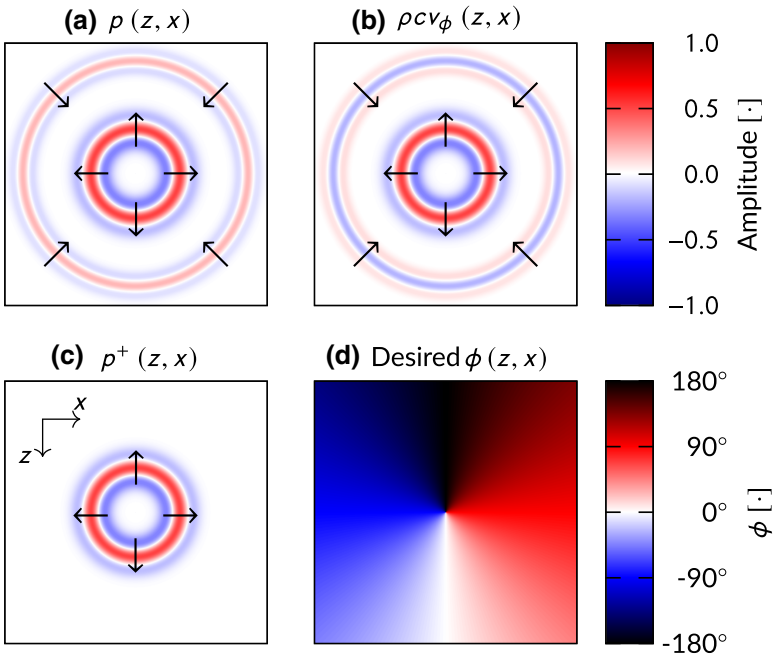

Figure 3 Directional decomposition of a pressure snapshot (a), consisting of an expanding wavefield (inner circle) and a collapsing wavefield (outer circle), by scaling the radial particle velocity (b) to (a), according to the desired decomposition direction (d), and adding the two to find the expanding pressure wavefield (c). Note that at the centre the wavefields were (up-left)-(down-right) decomposed and that the coordinate system displayed in (c) applies to all panels.

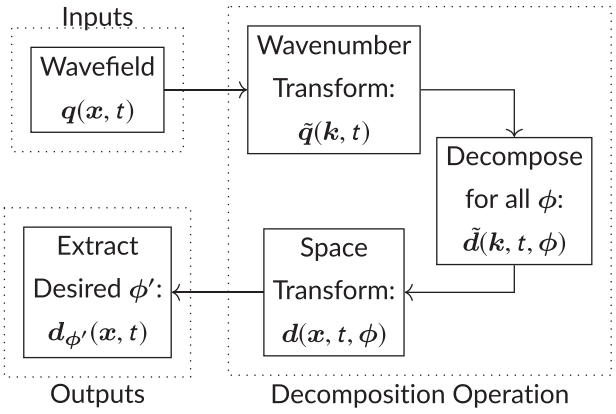

Figure 4 Concept behind having locally different decomposition directions.

2.7 Approximation for locally homogeneous media

Now that we have derived the decomposition for globally homogeneous media we extend it, in an approximate sense, to locally homogeneous media. To do this we apply the wavenumber scaling of the decomposition in the wavenumber domain and multiply with the local specific acoustic impedance in the space domain. We achieve this by transforming the decomposition operator in equation (34) back to the space domain. As the medium parameters are assumed to be globally homogeneous we can pull the Fourier transforms into the decomposition operator, equation (34), where they cancel for the first column, and sandwich the wavenumber fraction in the second:

$$\mathbf{L}_{p,z} = \frac{1}{2}\begin{pmatrix} 1 & \rho c \mathcal{F}_{\mathbf{x}}^{-1} \dfrac{||\mathbf{k}||}{|\kappa_z|} \mathcal{F}_{\mathbf{x}} \\ 1 & -\rho c \mathcal{F}_{\mathbf{x}}^{-1} \dfrac{||\mathbf{k}||}{|\kappa_z|} \mathcal{F}_{\mathbf{x}} \end{pmatrix}. \tag{48}$$

We can now let $\rho c = \rho(\mathbf{x})c(\mathbf{x})$ vary spatially in an approximation to decomposition in heterogeneous media. The decomposition is then as follows:

$$\begin{pmatrix} p_z^+ \\ p_z^- \end{pmatrix} = \frac{1}{2}\begin{pmatrix} 1 & \rho(\mathbf{x})c(\mathbf{x}) \mathcal{F}_{\mathbf{x}}^{-1} \dfrac{||\mathbf{k}||}{|\kappa_z|} \mathcal{F}_{\mathbf{x}} \\ 1 & -\rho(\mathbf{x})c(\mathbf{x}) \mathcal{F}_{\mathbf{x}}^{-1} \dfrac{||\mathbf{k}||}{|\kappa_z|} \mathcal{F}_{\mathbf{x}} \end{pmatrix} \begin{pmatrix} p \\ v_z \end{pmatrix}. \tag{49}$$

This approximation appears to be a relatively accurate decomposition that mimics plane-wave decomposition for heterogeneous media, as will be shown using synthetic examples later. It, however, does not take scattering properly into account, nevertheless it works very well for locally homogeneous media as we will demonstrate using synthetic examples in Section 4.

2.8 Steering the decomposition direction according to medium parameters

Allowing medium parameters to vary locally suggests that the decomposition direction could, in conjunction with

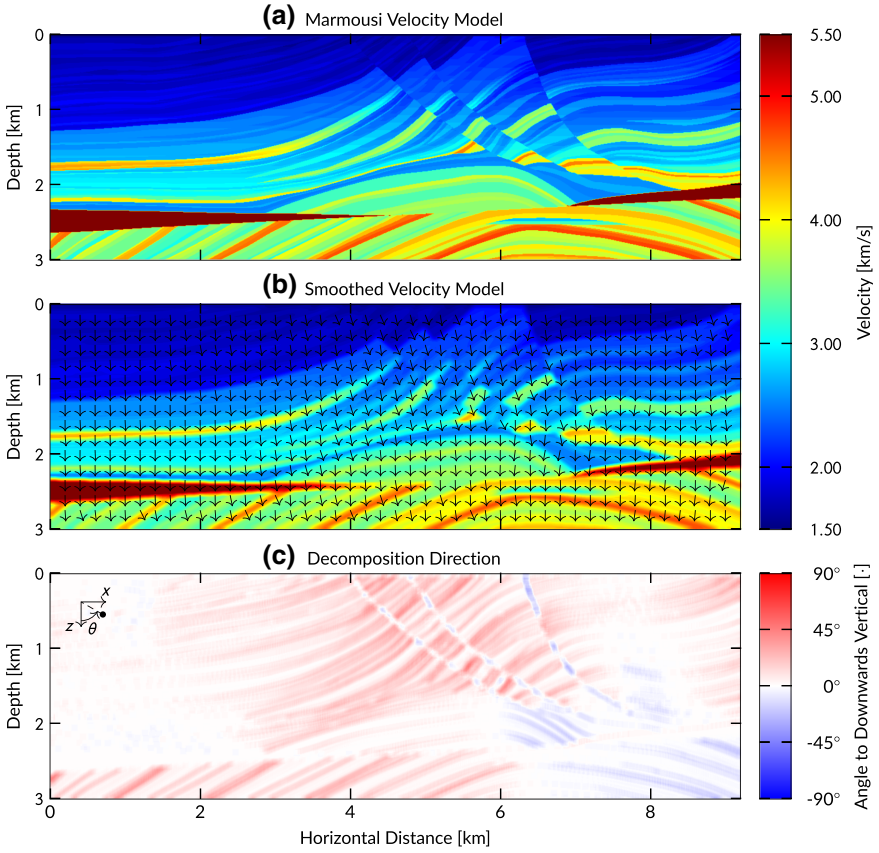

Figure 5 (a) Marmosui velocity model smoothed using a 10 × 10 grid-points moving-average filter (b) with associated downwards-pointing gradient-direction vectors, taken from decomposition direction map (c) used to steer directional wavefield decomposition.

Subsection 2.6, be tied to medium parameter variations. This for example would allow the decomposition direction to be normal to medium interfaces. This has ramifications for many acoustic processing techniques like imaging.

Given a snapshot of a wavefield in a known medium and Subsection 2.6, it is now possible to steer the decomposition based on local medium parameter gradients at a point to ensure that the decomposition direction is always parallel to variations in medium parameters. To do so one computes the gradients of the acoustic velocity and the density, from which one derives two normalized direction maps by dividing by the magnitude of the respective gradients. These direction maps can then be used to steer the decomposition, however, the direction based on these two maps may be multivalued as the gradients in the bulk density and medium velocity are not necessarily aligned. This can approximately be accounted for by calculating specific-acoustic-impedance-based directions as follows:

$$\mathbf{n} = \frac{\nabla \rho c}{||\nabla \rho c||}, \tag{50}$$

where the vector $\mathbf{n}$ is the normalized local specific-acoustic-impedance-based direction that can be expressed in terms of angles. Note that the decomposition direction is ill-defined where the gradient is zero. In this case the decomposition direction must be explicitly chosen.

Let us illustrate the concept with an example. Figure 5(a) shows the constant-density Marmousi velocity model (Brougois *et al.* 1990), and below it a smoothed version to avoid discontinuous decomposition directions (Fig. 5b), based on which ideal decomposition directions may be readily computed (Fig. 5c). Note that wherever the gradient was zero the decomposition direction was chosen to point downwards. The vector field in Fig. 5(b) shows coarsely the decomposition directions in Fig. 5(c), demonstrating that they are quasi-normal to velocity interfaces.

By tying the decomposition direction to local variations in medium parameters we can now approximately ensure that wavefields are decomposed into in- and out-going wavefields at an interfaces. This can improve acoustic processing techniques, like imaging, by ensuring that decomposition is always normal to medium interfaces.

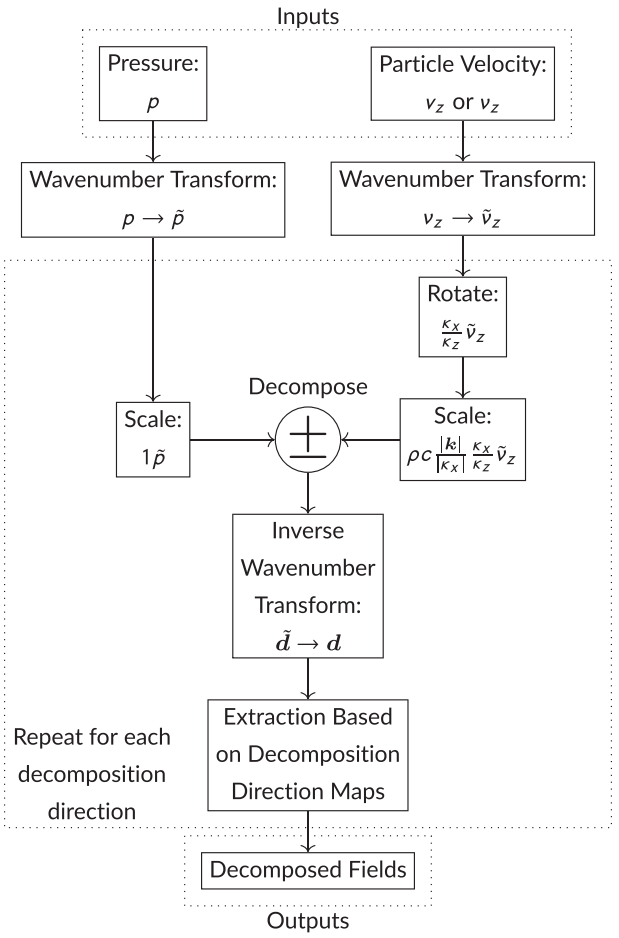

Figure 6 Workflow of directionally steered snapshot wavefield decomposition.

3 NUMERICAL IMPLEMENTATION

Implementation of snapshot wavefield decomposition for homogeneous media is simple in the wavenumber domain and can be used as an approximation for heterogeneous media. The general decomposition workflow, Fig. 6, for multicomponent homogeneous media data in a three-dimensional (3D) volume, is to transform the data to the 3D wavenumber-time domain. Then for each desired decomposition direction, not all decomposition directions as in Subsection 2.6, the wavefield is iteratively decomposed for each desired direction, after which the decomposed wavefields are transformed back to the space domain. At the end of each iteration only those points at which the current decomposition direction matches the desired decomposition at said point are kept. Thus the desired decomposed fields corresponding to the spatially varying decomposition direction is built up. This requires two forward spatial Fourier transforms, followed for each iteration by multiplication of the pressure and particle velocity with large diagonal operations to scale the transformed fields to each other for decomposition, depending on normalization, and two inverse Fourier transforms, followed by extracting desired decomposed points. Based on Fig. 6 this seems simple to implement, there are, however, some caveats.

In Subsection 2.6 we described how to achieve spatially varying decomposition directions. This required decomposing the wavefield according to all possible decomposition directions. This is numerically expensive. Hence, we suggest to precompute a list of desired decomposition directions, based on an impedance model for example. This list, if the decomposition direction angles are not strictly acute, is then scanned to eliminate decomposition directions pointing in opposite directions, as these can be computed simultaneously. To further reduce the workload the list of decomposition directions can be binned; later the decomposition results are then interpolated between their nearest bin centres.

It should be noted here that equation (50) can become numerically unstable if the gradient is very small due to the inherent limited numerical precision of floating point numbers on computers. For the case where the medium is homogeneous we suggest to define a desired direction. For regions where the direction may be numerically imprecise we suggest to either increase the floating point precision of the computation or to interpolate these values based on neighbours to at least ensure a smoothly varying decomposition direction. For our examples the used models were stored using 32-bit IEEE 754 floating-point numbers, while the gradient computations were done by increasing the precision of these numbers to double-precision 64-bit IEEE 754 floating-point numbers. This avoided numerical precision problems in computing the gradient.

For the interpretation of decomposed snapshots we suggest that the decomposition direction map is spatially smooth. The employed algorithm, however, can handle both smooth and non-smooth decomposition direction maps. Using smooth decomposition direction maps avoids sharp contrasts in decomposed amplitudes, while decomposed events remain continuous. This aids greatly in the visual inspection and interpretation of decomposed snapshots. Smooth decomposition direction maps can be computed with equation (50) by either using a smooth impedance model, as we have done in our examples, or by smoothing the direction map after computing it.

Note that the decompositions require Fourier transforms, which for discrete data are generally formulated as finite dense

circulant matrices acting on the whole domain under the assumption that the domain is periodic. This is generally inaccurate as it is implicitly assumed that the signal is periodic in space, suggesting the need for tapering at domain edges to avoid step discontinuities at model boundaries in the space domain and associated aliasing in the wavenumber domain. As we will demonstrate with the synthetic examples in Section 4 this is not strictly necessary but may improve results. In contrast to the Fourier transform the rotation and scaling operators are diagonal matrices and only suffer from incorrectly scaling spatially aliased signals.

Furthermore, for discrete data when the wavefield components do not lie on the same space-time grid it is imperative for best results that the two components are interpolated to lie on the same grid. This ensures that the associated temporal and spatial phase shifts between the signals do not contaminate the decomposition. We found for our synthetic finite difference examples that it was often acceptable to have the fields not on the same time grid, but they had to be on the same space grid. This is a function of the signal bandwidth in the wavenumber and frequency domains. The wider the bandwidth and the closer these were to modelling limits, like the Courant number, the larger the error grew.

For all the figures in this work we shifted the particle velocities onto the pressure grid in the wavenumber domain by multiplying in two spatial dimensions the horizontal particle velocity by $\exp(-ik_x\Delta x/2)$, where Δx is the horizontal grid spacing, and the vertical particle velocity by $\exp(-ik_z\Delta z/2)$, where Δz is the vertical grid spacing. We also found that it was often also acceptable to simply linearly interpolate the particle velocities onto the pressure grid. This can be significantly faster and does not suffer from the inherent wrap-around effect of most discrete Fourier transforms, the resulting amplitudes however are often less accurate. To interpolate the particle velocity to the same time grid we used half the time derivative of the particle velocity at every time instance, which is a by-product of using a staggered finite difference scheme to step wavefields forward in time. As we often found that this is unnecessary for acceptable results in practice, all figures in this work show decomposed results without interpolating either the pressure or particle velocities onto the same time grid. Note that we do not suggest to shift staggered wavefields onto the same time grid in the frequency domain as this removes the advantage of this method of being able to act exclusively on snapshots of a wavefield.

For waves travelling at near-right angles to the decomposition direction, the wavenumber scaling in, for example, equation (22) may become numerically unstable. In this case it is advantageous to cast the problem in terms of the magnitude of the particle-velocity vector, equation (28). Using the magnitude of the particle velocity in two dimensions (2D) comes at the cost of requiring an additional spatial Fourier transform over the other component of the particle velocity.

We would like to conclude this section with a discussion on the numerical aspects of the decomposition algorithm, which is dominated by the Fourier transforms. In our case these were implemented through the FFTW 3.3.6-pl2 library (Frigo and Johnson 2005). The compute time of the Fast Fourier Transforms (FFT) are expected to scale with $n\log(n)$, where n is the number of data points to be Fourier transformed. As such we expect the compute time of the decomposition algorithm, when decomposing along one direction, to scale in the same fashion. When decomposing along many directions the compute time is expected to linearly increase with the number of directions to decompose along, as an additional Fourier transform is needed per additional direction. Although all examples in this work are in two spatial dimensions, decomposition in three spatial dimensions is also feasible. This comes at the cost that the algorithms compute time is expected to increases approximately proportionally to n_3, the number of elements in the third spatial dimension, with respect to a two-dimensional model that has the same size in the first two dimensions. When decomposing while modelling in a high-performance computing setting, the decomposition step can be offloaded to other compute nodes or dedicated FFT hardware to reduce the impact of the decomposition on the modelling time, when decomposing while modelling. Alternatively the decomposition operator can be reduced in size, written in the space domain and then iteratively convolved with the snapshot to decompose it. This reduces accuracy, especially for waves travelling nearly perpendicular to the decomposition direction.

In order to compare compute times, the average decomposition times for 100 one-dimensional (1D), 2D and 3D snapshots were determined, where each dimension had a size of 1000 points. We used a single thread without vectorization on a stock Xeon E5-2680 v3 central processing unit. The system's random access memory consisted of eight 32 GB Samsung M393A4K40BB1-CRC modules at 2133 MHz with default settings in a dual channel configuration. The average compute times for the 1D, 2D and 3D snapshots are 6 μs, 15 ms and 29 s respectively. Between the 1D and 2D cases we expected a 2000 fold increase, while between the 2D and 3D cases we expected a 1500 fold increase. The above tests were assuming only one decomposition direction, but when 99 additional decomposition directions are also included, the

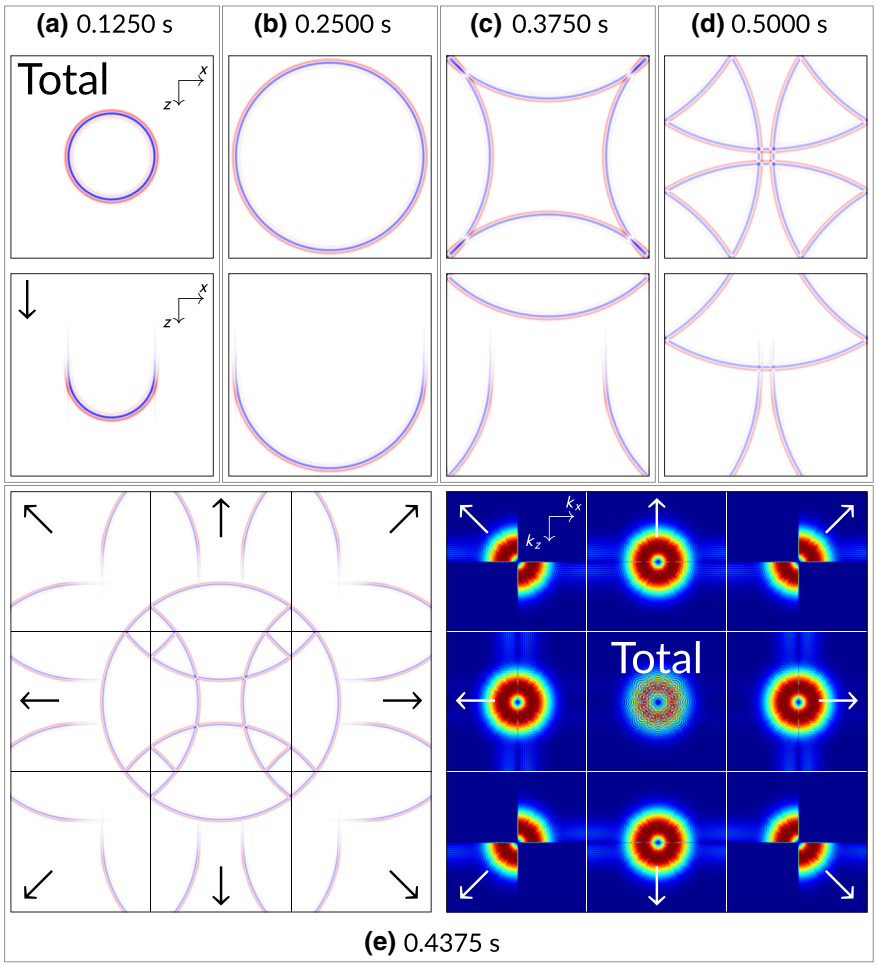

Figure 7 Homogeneous acoustic wavefield decomposition on a 500 m × 500 m 1 km s^{-1} homogeneous model. The top row of (a)–(d) shows the total pressure snapshots decomposed into down-going snapshots below. (e) shows a snapshot of the total pressure at 1.75 s directionally decomposed into quadrants. (f) displays the corresponding wavenumber spectra, with the images centred on the origin. Note that the wavefields were decomposed in the wavenumber domain, and therefore low wavenumber decomposition artefacts can be observed as vertical and horizontal bands. Furthermore the coordinate displayed coordinate systems in (a) also apply to (b, c and d), while the coordinate systems in the upper left panels of (e) and (f) apply to all panels in (e) and (f) respectively.

compute times increase accordingly. Assuming we take 100 different directions, requiring 101 Fourier transforms, the average compute time of the 2D snapshots increased to 754 ms. For the 3D case the average compute time was 1460 s. Note that these values are only indicative and can vary between compute systems.

4 SYNTHETIC EXAMPLES

We now show synthetic examples to illustrate the theory and concepts discussed earlier. We begin with a constant-density constant-acoustic-velocity example and move on from there to a layered model, with velocity and density variations, and from there to the heterogeneous velocity Marmousi model. We demonstrate on these models the various decompositions and their characteristics.

4.1 Constant-parameter model

To illustrate the simplest case of decomposition, we choose a model where the density is constant at 1000 kg m^{-3} and the medium velocity is 1 km s^{-1}. The grid is 500 m × 500 m discretized with a 1 m sampling rate, and a 60 Hz peak frequency Ricker wavelet, sampled every 0.5 ms, is injected as a volume injection source at the centre of the model with a 0.0175 s time delay. Figure 7 displays snapshots of said

wavefield. Figures 7(a-d) show advancing snapshots of the wavefield, decomposed into down-going wavefields below. Figure 7(e) shows a snapshot between Figures 7(c,d) in time on the left. Now, however, the snapshot has not only been up–down decomposed but also left–right, as indicated by the arrows in the different panels. To the right of the decomposed snapshots are the corresponding amplitudes of the snapshots around the origin in the wavenumber domain.

The total wavefields, the central panels in Fig. 7(e,f), were first decomposed using equation (23), zeroing the horizontal or vertical wavenumbers as applicable. To compute the wavefields travelling in quadrants the total wavefield was also decomposed into up- and down-going particle-velocity-normalized wavefields. These were rotated using equation (26) to find the up- and down-going horizontal particle velocities. These in turn were then used in conjunction with the up- and down-going pressure to decompose the wavefields again into left- and right-going wavefields.

Consider the wavenumber spectrum of the total field, central panel of Fig. 7(f), which has a jittery amplitude behaviour due to the interferring waves in the central pane of Fig. 7(e). Wavefields propagating in opposite directions are destructively interfering, causing the amplitude of the total wavefield to be smaller than that of the decomposed fields. Furthermore, the amplitude distribution in the total field around the origin is not as clear as for the decomposed fields. After decomposition it is much clearer, however, that edge-related artefacts and artefacts due to the asymptotic scaling of the particle velocity are also boosted. The amplitude spectra of the decomposed fields appear identical, however, the dominant difference between the decomposed fields is in the phase (not shown). This is expected as the wavefield radiated spherically away from the source at the centre. Further decomposing the wavefield corresponds to a simple quadrant mute in the wavenumber domain. Note that the decomposition order is highlighted by the horizontal erroneous bands due to asymptotic scaling. These bands would have been vertical if the wavefield had been first left–right decomposed and then up–down.

4.2 Constant parameter model: comparison of different scalings

To illustrate the possible numerical errors introduced by using the wavenumber-based scaling of equation (22), as opposed to the magnitude of the particle-velocity vector, equation (28), see Fig. 8. Figure 8(a,b) shows the pressure and specific-acoustic-impedance-scaled vertical particle velocity due to a sum of unit-amplitude Ricker-wavelet plane waves, travelling from left to right with increasing obliquity to the vertical axis. Figure 8(c,d) shows the corresponding amplitudes around the origin (centre of panel) in the wavenumber-time domain. Note that the vertical particle velocity (Fig. 8d) is missing the horizontally travelling wave corresponding to the horizontal red line segment in (Fig. 8c), see black ellipse.

We now scale the vertical particle velocity to the pressure using equations (22) and (28), resulting in Fig. 8(e,f). Note that the scaled vertical particle velocity is set to zero for $k_z = 0$. When comparing Fig. 8(e,f) to Fig. 8(c,d) the amplitudes of Fig. 8(c,f) are very similar, except where $k_z = 0$, while the amplitudes of Fig. 8(e) diverge from those in Fig. 8(f) away from the origin as one approaches $k_z = 0$. The reasons for this divergence are twofold: (1) numerical accuracy of the asymptotic wavenumber scaling in equation (22) degrades as one approaches $k_z = 0$, resulting in horizontal artefacts as can be seen in the dashed circles in Fig. 8(g,h), and (2) aliasing due to the finite size of the domain causes wrap-around artefacts due to the cyclic nature of the employed Fourier transform, as can be seen in the spy-glasses in Fig. 8(g,h). The aliasing causes high wavenumbers to map to lower wavenumbers, and vice versa, which are subsequently incorrectly scaled. It is suspected that one does not see this effect in Fig. 8(h) because the aliasing in the horizontal and vertical wavenumber for a given point in the wavenumber-time domain, when used to calculate the magnitude of the particle velocity, are equal/similar to the aliasing for the pressure at said point. It appears that using the magnitude of the particle velocity for decomposition on finite non-periodic domains is less corrupted by aliasing artefacts, suggesting that equation (28) should be used over equation (22) whenever possible.

4.3 Four-layer model

In the previous examples, we did not show the effect of variations in medium parameters on the model. Figure 9 shows up–down decomposed wavefields for a four-layer model, with a density increase, velocity increase and constant specific-acoustic-impedance interface from top to bottom, as shown in Fig. 9(a). Figure 9(b) shows a pressure snapshot, due a volume injection source at the origin injecting a 50 Hz Ricker wavelet, at 0.1 s. Figure 9(f) shows the corresponding recorded wavefield at a depth of 150 m, indicated by the dashed line in Fig. 9(b–d). Note that the top and bottom boundaries are both free surfaces while the left and right boundaries are absorbing, more precisely they are 500-element-wide perfectly matched layer boundaries (Chew and Liu 1996).

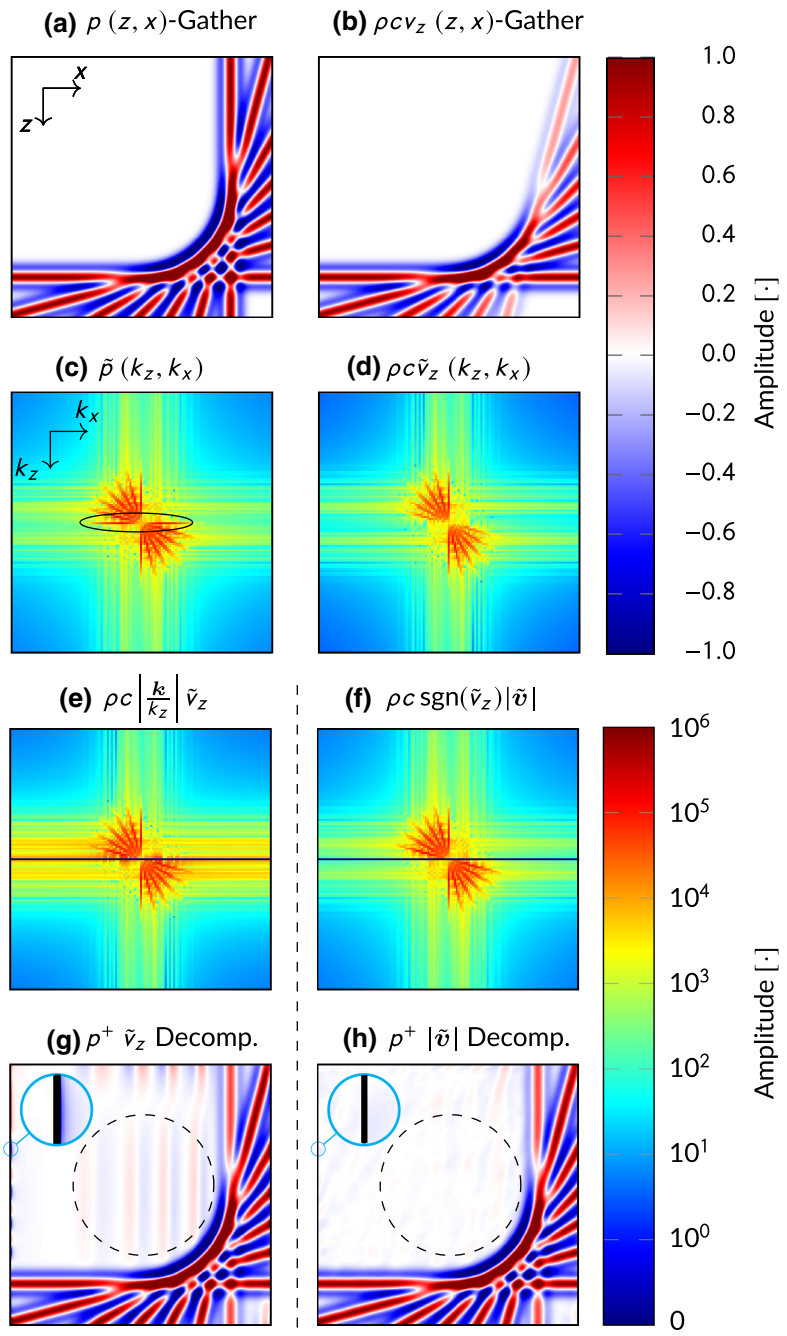

Figure 8 (a) Superposition of pressure plane waves at 0°, 15°, 30°, 45°, 60°, 75° and 90° to the vertical with the (b) associated specific-acoustic-impedance-scaled vertical particle velocity. (c) and (d) are extracts around the origin of the the magnitude of the wavenumber transforms of (a) and (b) respectively. (e) and (f) show scaled version of (c) and (d) according to equations (22) and (28) respectively. The fields were muted where $k_z = 0$. (g) and (h) show the corresponding decomposed wavefields in the space domain. Please note that in all panels the origin is at the centre of the image and that the coordinate system displayed in (a) applies to (a, b, g and h), while the coordinate system shown in (c) applies to (c–f).

The wavefields in Fig. 9(b,f) were then decomposed, using equations (23) and (28), into down-going waves in Fig. 9(c,g) and Fig. 9(d,h) respectively. Figure 9(e) shows the up-going pressure wavefield based on equation (23). Note that all panels were tapered at the edges to avoid the Gibbs–Wilbraham phenomenon. Please also note that the amplitudes have been clipped at 5% of the maximum to illustrate that the errors are generally smaller than 1%.

Comparing Fig. 9(b–d), the large vertical artefacts in Fig. 9(c) are immediately evident. These are caused by the incorrect scaling of small vertical wavenumbers due to aliasing artefacts because of the implicit fast Fourier transform jump-discontinuity at the surface. These artefacts are much smaller in Fig. 9(d). However, small artefacts associated to small vertical wavenumbers are visible throughout Fig. 9(c). It is suspected that these are caused by the interaction of

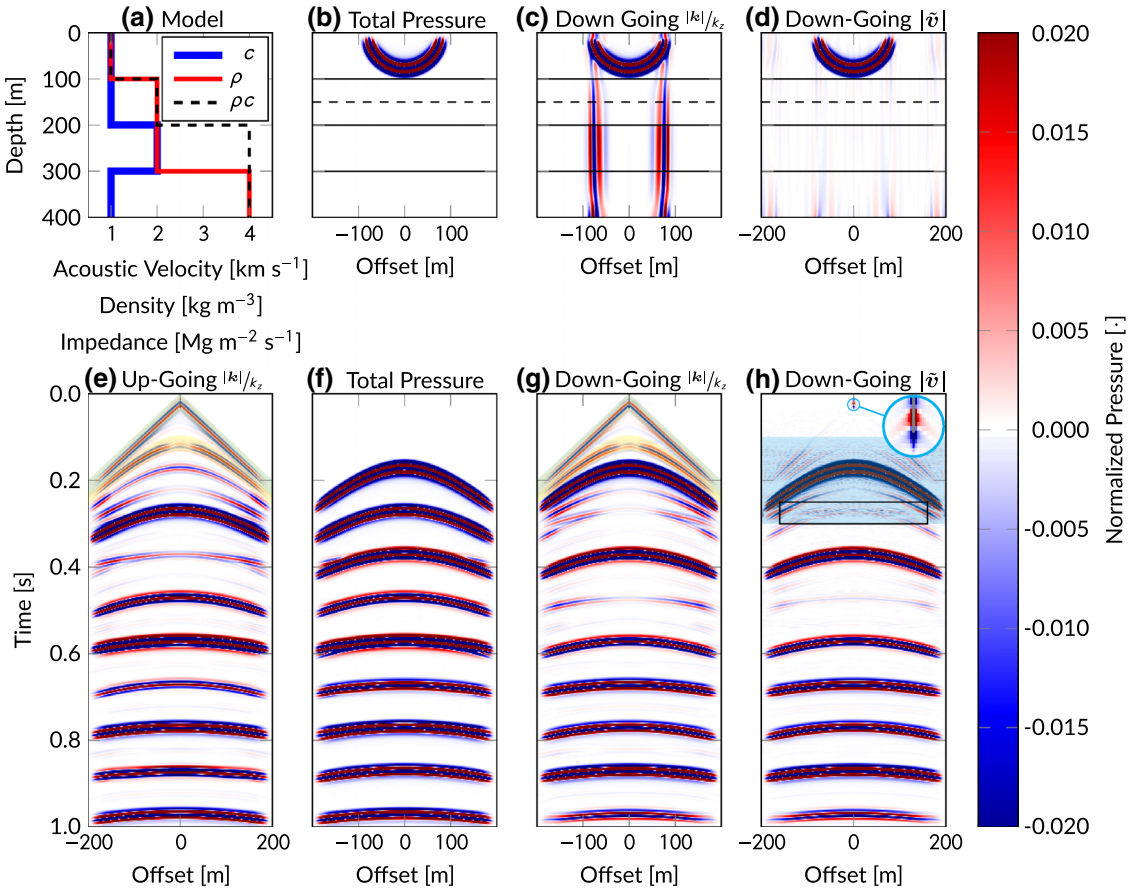

Figure 9 Pressure snapshot (b) from a four-layer model (a) decomposed into down-going waves by either scaling the vertical particle velocity in the wavenumber domain according to equation 23(c), or by using the magnitude of the particle-velocity vector according to equation 35(d). (f–h) show the corresponding wavefields recorded on the dashed surfaces in (b–d), while (e) shows the up-going wavefield, found by subtracting (g) from (f) and dividing by two.

aliasing, among other possible errors, of the horizontal and vertical particle velocity. They are also in part due to the heterogeneous medium.

We can see the same artefacts in Fig. 9(e,g,h), where the vertical bands in Fig. 9(c) now appear as an erroneous event in Fig. 9(e,g) that resembles a conventional direct wave when the source is at the same depth level as the acquisition surface, see shaded green area. When comparing Fig. 9(g,f) there is another event that arrives in Fig. 9(g) before the direct wave in Fig. 9(f), see yellow area. This event is associated with the erroneous vertical bands that arise due to the amplitude discontinuity when the wavefield reflects at the first interface, similar to the two vertical artefacts due to the tapered edge discontinuity at the top of the model causing two erroneous vertical events in Fig. 9(c). These errors are mostly absent from Fig. 9(h), they are only visible in time from about 0.1 s to 0.3 s, the cyan area, along with other noise, in the form of high-frequency noise. This noise is most evident inside the black box. Evidently decomposition in terms of the magnitude of the particle velocity, equation (28), is not as sensitive to these errors as decomposition in terms of equation (23).

Figure 9(h), however, suffers from other errors. Between 0.1 s and 0.3 s there appears the aforementioned high-frequency noise, see cyan area. This noise is again due to the interaction of artefacts in both the horizontal and vertical particle velocity. If the model domain is made larger these become smaller, but they do not completely vanish as they are also partially due to the variations in medium parameters, which are quite strong for this model. Qualitatively decomposing in terms of the magnitude of the particle-velocity vector, Fig. 9(h), appears to perform better than only scaling the vertical component of the particle velocity in the decomposition,

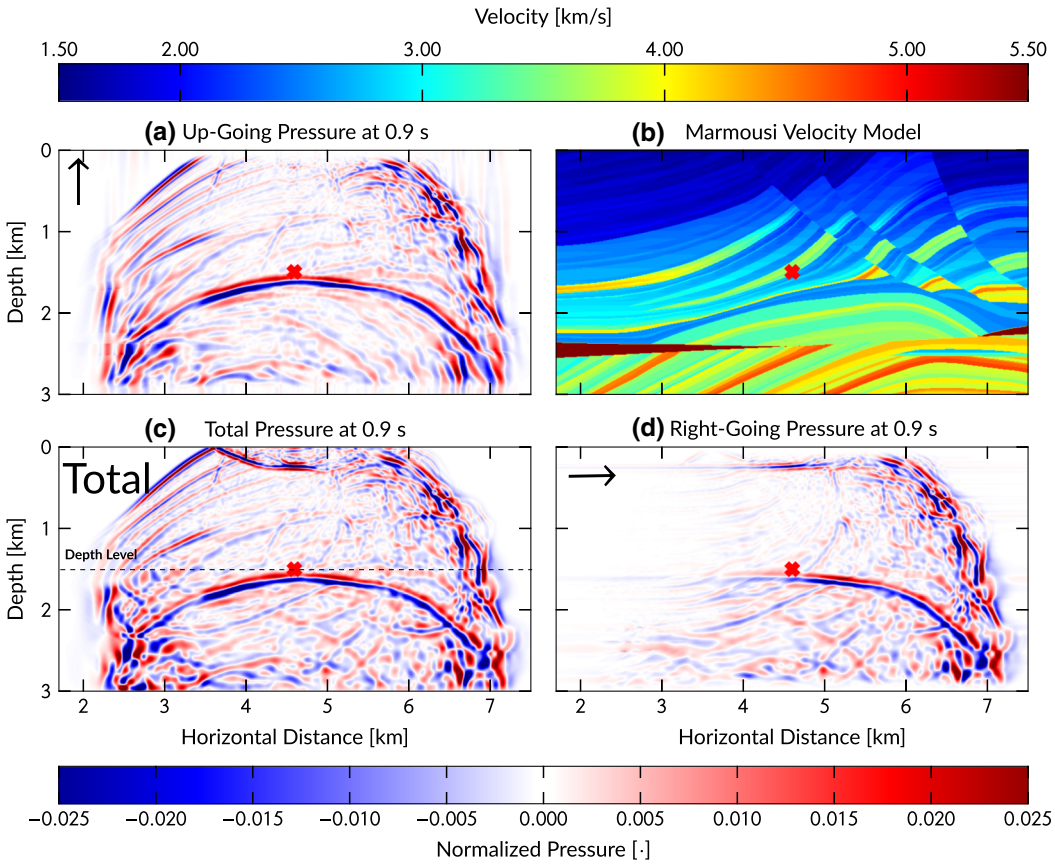

Figure 10 Pressure snapshot (c), from the constant-density Marmousi model (b), directionally decomposed into up- (a) and right-going (d) pressure-normalized wavefields. The source location is indicated by a red cross. Amplitudes are normalized to the unit amplitude Ricker source wavelet.

Fig. 9(g), when compared to conventional surface normal decomposition, which is ideal for this scenario. The errors are more concentrated in Fig. 9(g) though.

Note that both Fig. 9(h,g), as well as conventional decomposition, show errors around the source if it is not explicitly included in the decomposition scheme. This can be seen in the spyglass in Fig. 9(h). In this case these errors have two components, the source itself, which was not properly accounted for, and the fact that the data were modelled using a staggered-grid finite-difference scheme, where the wavefield mismatch in space and time between the pressure and particle velocity is largest around source locations.

4.4 Marmousi model: (Up-left)-(down-right) decomposition

We have demonstrated that snapshot decomposition performs well on layered models. Let us now relax the lateral-homogeneity condition and consider fully heterogeneous velocity models. Figure 10 shows in the upper right the Marmousi velocity model (Fig. 10 b), with the source location marked using a red cross. In this case a 50 Hz Ricker wavelet was injected. Figure 10(c) shows the total pressure wavefield for a snapshot at 0.9 s. The other two panels shows the pressure wavefield decomposed into up- and right-going waves, Fig. 10(a,d) respectively. In this case the wavefields were decomposed using equation 23, including the use of the horizontal particle velocity to account for horizontally travelling waves. Interesting here is to look at the curvature of the dominant events, and to see that they are well decomposed. The unexepected vertical and horizontal events in Fig. 10(a,d) respectively are caused by the incorrect scaling due to the asymptotic nature of equation (23) and the inherent incorrect scaling of aliased waves due to the heterogeneous nature of the model. As there is no reference decomposition for a model of this complexity, it is difficult to grade the accuracy of the decomposition. Overall and when seen from one snapshot to another the decomposition appears to do well.

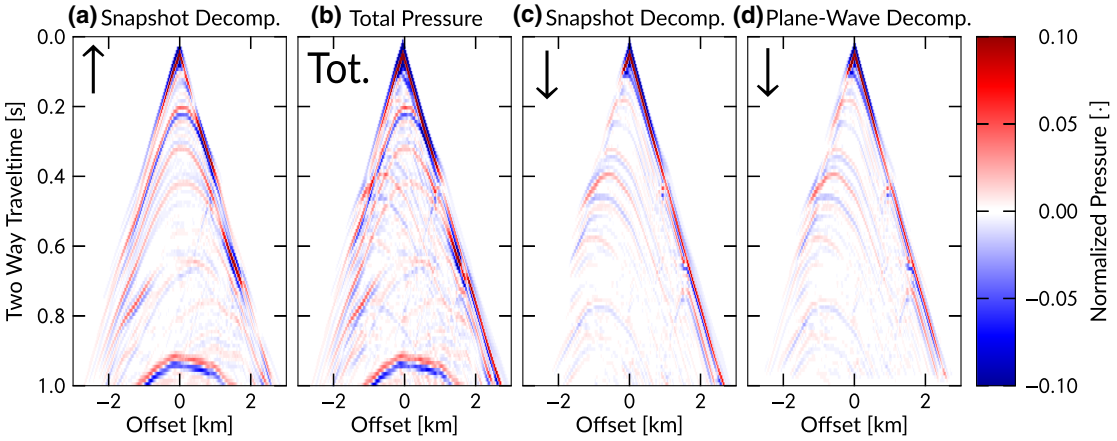

Figure 11 Directionally decomposed common-shot gathers, from the Marmousi model, through the source depth level, indicated in Fig. 10. On the far right is the down-going resampled plane-wave decomposed reference response (Suprajitno and Greenhalgh 1985), which was tapered at the bottom.

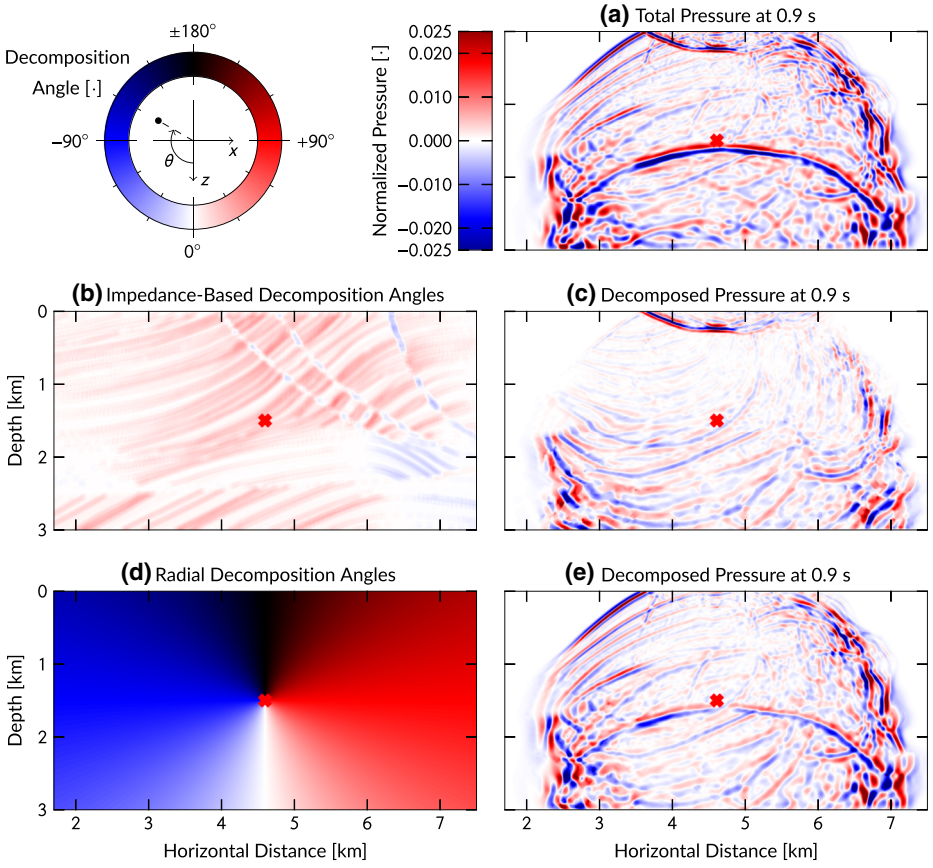

Figure 12 Acoustic wavefield propagated from the center of the Marmousi model, see Fig. 5 for the velocity model, decomposed along variations in the impedance and radially away from the source. (a) shows the total pressure wavefield 0.9 s after source excitation; the source location is indicated by a red cross. (b) and (d) show the decomposition angles parallel to impedance variations and radially away from the source location. (c) and (e) show the corresponding decomposed pressure-normalized wavefields according to the angles in (b) and (d) respectively. Note that for (e) the wavefield at the source location was not decomposed as any wavefield at the source location must propagate away from it. Note that amplitudes are normalized to the unit amplitude Ricker source wavelet.

Figure 11 allows us to compare decomposed common-shot gathers at the source depth level, which were decomposed using equation (35) at every time sample. We can see that we are able to nicely decompose the wavefield. Comparing the down-going wavefield to the plane-wave down-going reference response, one finds they are nearly identical, except from at the bottom of the panels, because the plane-wave decomposed panel was tapered at the top and bottom to avoid wrap-around artefacts. Note that for very early times the wavefield was not decomposed, as source artefacts were too dominant, due to the fact that the source was not taken into account in the decomposition.

4.5 Marmousi model: Impedance-based decomposition-direction steering

We have demonstrated that wavefields propagating in the Marmousi model can be easily decomposed along spatially invariant directions. We can take the decomposition a step further by decomposing in the direction normal to medium interfaces, as discussed in Subsection 2.8. Figure 12 shows the decomposition results, found using equation (47), associated to the proposed decomposition directions in Fig. 5, which were computed using equation (50). Figure 12(c) shows the down-going interface-normal decomposed pressure-normalized wavefield. This decomposed wavefield, although very similar to the normal down-going pressure wavefield, is important for imaging with acoustic wavefields.

As Fig. 12(c) is difficult to interpret with respect to the prescribed decomposition direction, Fig. 12(d) shows desired decomposition directions radiating away from the source location. Using these directions we would then decompose the wavefield into waves travelling away from and towards the source. If one follows the curvature of the wavefronts in Fig. 12(e), one can clearly see that they suggest the wavefield is propagating away from the source, with the exception of the dominant wave travelling upwards. This wave, however, is also travelling away from the source, its propagation angle is just nearly at a right angle to the decomposition direction. The wave vanishes right below the source as there it is propagating towards the source.

5 DISCUSSION AND CONCLUSION

Conventional up–down wavefield decomposition is applied to wavefields recorded on horizontal surfaces to decompose into wavefields propagating up and down. This study took a different approach to conventional wavefield decomposition and derived operators that decompose wavefields at one instance in time that are known everywhere in space, effectively using a temporal surface instead of a spatial surface. This has advantages and disadvantages when compared to conventional decomposition.

Its biggest disadvantage is that the decomposition does not correspond to how acoustic data is generally acquired, which is generally on a single surface and not everywhere in space for one instance in time. This implies that this method is better suited for other applications, like decomposing wavefields as they are being modelled, for example using finite-difference schemes, to improve reverse time migration (RTM) imaging results, see Díaz and Sava (2015). This is where the proposed approach excels as the wavefield is known everywhere from one time step to the next, allowing for directional wavefield decomposition at every time step, as opposed to having to record the wavefield and then later decompose it using conventional decomposition along some surface.

Another advantage over conventional decomposition is that in conventional decomposition the decomposition direction is always normal to the surface along which the decomposition occurs, whereas for the proposed scheme the wavefield can be decomposed into any direction. The same is achievable using conventional decomposition if the wavefield is known everywhere in space and time. Hence, the proposed scheme is ideal for any algorithms based on snapshots of a wavefield like RTM, which would benefit from the ability to locally decompose wavefields normal to interfaces, not just between in- and out-going wavefields but also according to the quadrant from which the wave arrives using sub-decomposition.

ACKNOWLEDGEMENTS

We wish to especially thank Reynam Pestama for fruitful suggestions on this work and Jan Willem Thorbecke, upon whose finite-difference code Fdelmodc (Thorbecke and Draganov 2011) much of this work is based.

ORCID

Max Holicki http://orcid.org/0000-0002-3947-011X
Guy Drijkoningen http://orcid.org/0000-0001-8232-2449
Kees Wapenaar http://orcid.org/0000-0002-1620-8282

REFERENCES

Aki K. and Richards P.G. 1980. *Quantitative Seismology: Theory and Methods*, Vol.1. W.H. Freeman.

Barr F. and Sanders J. 1989. Attenuation of water-column reverberations using pressure and velocity detectors in a water-bottom cable. SEG Technical Program Expanded Abstracts, 653–656.

Brougois A., Bourget M., Lailly P., Poulet M., Ricarte P. and Versteeg R. 1990. Marmousi, model and data. *EAEG Workshop-Practical Aspects of Seismic Data Inversion*, Copenhagen, Denmark, May 1990. European Association of Exploration Geophysicists.

Chew W. and Liu Q. 1996. Perfectly matched layers for elastodynamics: a new absorbing boundary condition. *Journal of Computational Acoustics* **4**, 341–359.

Dankbaar J. W. M. 1985. Separation of P- and S-waves. *Geophysical Prospecting* **33**, 970–986.

Díaz E. and Sava P. 2015. Understanding the reverse time migration backscattering: noise or signal? *Geophysical Prospecting* **64**, 581–594.

Frasier C. 1970. Discrete time solution of plane P-SV waves in a plane layered medium. *Geophysics* **35**, 197–219.

Frigo M. and Johnson S. 2005. The design and implementation of fftw3. *Proceedings of the IEEE* **93**, 216–231.

Kennett B. 1984. An operator approach to forward modelling, data processing and migration. *Geophysical Prospecting* **32**, 1074–1090.

Leaney K. and Schlumberger E. 1990. Parametric wavefield decomposition and applications. 1990 SEG Annual meeting, San Francisco, CA, Expanded Abstracts, 1097–1100.

Lu S., Whitmore D., Valenciano A. and Chemingui N. 2015. Separated-wavefield imaging using primary and multiple energy. *The Leading Edge* **34**, 770–778.

Poynting J. 1884. On the transfer of energy in the electromagnetic field. *Philosophical Transactions of the Royal Society of London* **175**, 343–361.

Shen P. and Albertin U. 2015. Up-down separation using hilbert transformed source for causal imaging condition. SEG Technical Program Expanded Abstracts, 4175–4179.

Suprajitno M. and Greenhalgh S. 1985. Separation of upgoing and downgoing waves in vertical seismic profiling by contour-slice filtering. *Geophysics* **50**, 950–962.

Thorbecke J. and Draganov D. 2011. Finite-difference modeling experiments for seismic interferometry. *Geophysics* **76**, H1–H18.

Ursin B. 1983. Review of elastic and electromagnetic wave propagation in horizontally layered media. *Geophysics* **48**, 1063–1081.

Wapenaar C., Herrmann P., Verschuur D. and Berkhout A. 1990. Decomposition of multicomponent seismic data into primary P- and S-wave responses. *Geophysical Prospecting* **38**, 633–661.

White J. E. 1965. *Seismic Waves; Radiation, Transmission, and Attenuation*. McGraw-Hill, New York.

Yoon K. and Marfurt K. 2006. Reverse-time migration using the poynting vector. *Exploration Geophysics* **37**, 102–107.

